Title

Numerical investigation of heating and cooling-induced damage and brine migration in geologic rock salt : Insights from coupled THM modeling of a controlled block scale experiment



Authors

Tounsi, H

Rutqvist, J

Hu, M

et al.

Publication Date

2023-02-01

DOI

10.1016/j.compgeo.2022.105161

Computers and Geotechnics 154 (2023) 105161

Contents lists available at ScienceDirect

Computers and Geotechnics

journal homepage: www.elsevier.com/locate/compgeo

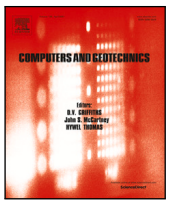

# Numerical investigation of heating and cooling-induced damage and brine migration in geologic rock salt : Insights from coupled THM modeling of a controlled block scale experiment

H. Tounsi [a], J. Rutqvist [a,*], M. Hu [a], R. Wolters [b]

[a] Energy Geosciences Division, Lawrence Berkeley National Laboratory, Berkeley, CA 94720, USA
[b] Chair for Geomechanics and Multiphysics Systems, Clausthal University of Technology, Erzstr. 20, D-38678 Clausthal-Zellerfeld, Germany

ARTICLE INFO

*Keywords:*
Numerical modeling
THM coupling
Rock salt
Brine inflow
Heating/cooling damage
Permeability increase

ABSTRACT

Controlling brine flow is important for the safe disposal of radioactive waste in salt rocks. Thermal and mechanical processes can have a significant impact on brine flow, although this has never been thoroughly investigated. In this study, we conduct fully coupled THM modeling for analyzing brine flow in rock salt, considering non-isothermal two-phase flow through deformable porous media. To rigorously represent rock salt behavior, we incorporate suitable phenomenological models for creep and shear and tensile-induced dilatancy/damage, and their effect on the flow properties. To validate such a complex model, we use it to analyze an experiment on a meter-scale salt block subjected to multistage heating and cooling under controlled laboratory conditions. The experimental data and our model predictions of temperature and brine inflow show good agreement. Our modeling shows that it is important to consider the coupling between the heating- and cooling-induced damage and the flow properties for rigorously estimating brine inflow. Based on our modeling, a cooling-induced brine inflow spike is caused by a permeability increase due to tensile dilatancy. Thus, our modeling will be useful for a proper design of a cooling phase in the salt repositories to avoid or minimize damage and the resulting brine inflow.

## 1. Introduction

Rock salt has long been recognized as a promising medium for geologic disposal of nuclear waste because of its naturally low permeability, relatively high thermal conductivity and its self-sealing capacity (Sweet and McCreight, 1983; Cosenza et al., 1999; Winterle et al., 2012; Chen et al., 2013). However, the formation of micro-fractures in the salt host rock may compromise the short-term hydraulic integrity of the disposal facility since they are prone to coalesce and can, therefore, provide pathways for brine migration (Hansen and Leigh, 2011). Multiple laboratory and *in situ* tests have shown that rock salt micro-fracturing is often initiated by the two following phenomena: shear-induced dilatancy (Stormont, 1997; Schulze et al., 2001) and/or tensile stresses exceeding the tensile strength of salt, which is relatively low, around 1 MPa (Hoffman and Ehgartner, 1998; Wisetsaen et al., 2015).

Micro-fracturing by shear-induced dilatancy initiates upon the excavation of drifts and boreholes, around which a disturbed rock zone (DRZ) develops and grows (Hansen, 2008). This zone is characterized by low pore pressure and large deviatoric stresses that exceed the so-called dilatancy boundary, leading to dilation-induced micro-fractures that result in an increase of permeability and porosity as well as a decrease of air-entry pressure (Stormont et al., 1992; Stormont, 1997; Beauheim and Roberts, 2002). The result is a short-term redistribution of brine and gas saturations and a brine inflow into the excavation, which magnitude is controlled by the competition between the creation and creep closure of dilation-induced micro-fractures.

Tensile fracturing associated with high pore pressure or sharp temperature drops are known processes in a number of geoengineering applications. Thermal fracturing is sometimes used deliberately, for example, to enhance the permeability and injectivity of geothermal system reservoirs (Zhang et al., 2020). In cases when the host rocks are intended for a barrier or seal against fluid migration, such as in subsurface gas storage and nuclear waste disposal, tensile fracturing is highly undesirable. In the case of gas storage in underground salt caverns, for instance, it has been demonstrated that thermal cycling associated with frequent fluid injection and withdrawal can lead to the appearance of tensile zones that could jeopardize the mechanical stability and sealing capacity of the caverns (Rouabhi et al., 2017). For nuclear waste disposal in salt formations, several lab and field tests

* Corresponding author.
*E-mail address:* jrutqvist@lbl.gov (J. Rutqvist).

https://doi.org/10.1016/j.compgeo.2022.105161
Received 28 August 2022; Received in revised form 20 November 2022; Accepted 26 November 2022
Available online 8 December 2022

have been conducted to characterize the macroscopic movement of brine in rock salt under isothermal and heated conditions (e.g., Avery Island *in situ* brine inflow test (Krause, 1983), brine inflow experiments in a potash mine in New Mexico (Ewing, 1981; Shefelbine, 1982), 1-kg lab test (Hohlfelder and Hadley, 1979), Salt Block (SB) lab experiment II (Hohlfelder, 1980), Waste Isolation Power Plant (WIPP) *in situ* moisture release experiments (McTigue and Nowak, 1987; Finley et al., 1992) and Asse mine *in situ* brine migration tests (Coyle et al., 1987)). Kuhlman and Malama (2013) provides a comprehensive historical review of these tests and confront their key findings. In the absence of heating, the brine inflow response varies from one experiment to the other mainly due to the heterogeneity of the tested rock salt formation that the excavation intersects, as observed in the small-scale brine inflow experiment conducted at WIPP (Finley et al., 1992). This WIPP experiment provided brine inflow measurements over three years for 17 unheated vertical and horizontal boreholes intersecting different geologic units. Analysis of the collected data showed that boreholes located in a pure halite unit remained dry. In all other boreholes, inflow generally peaked after drilling and slowly decayed before reaching a nearly constant inflow rate that correlated with the type and width of non-salt layers (clay and anhydrite). In the presence of a heating phase, all the experiments show that brine inflow rates increase with an increasing borehole temperature (Hohlfelder and Hadley, 1979; Hohlfelder, 1980; Ewing, 1981; McTigue and Nowak, 1987). Also, and perhaps most importantly, several of these tests have shown that a considerable, if not the largest, amount of brine was released during the heater shut-down (Hohlfelder and Hadley, 1979; Ewing, 1981; Coyle et al., 1987) or sometimes during a cooling phase following the heating phase (Hohlfelder, 1980). A portion of this accumulated brine could be due to fluid inclusions that may migrate towards the heat source (Hu and Rutqvist, 2020).

In brief, fluid flow is particularly complex in salt host rocks, whether it be in isothermal conditions or in the presence of high thermal gradients, and cannot be accurately predicted without considering the creep of salt, which is a result of complicated microscale mechanical and chemical processes (Hu et al., 2021), and the strong coupling between thermal, hydraulic and mechanical processes.

Although several brine-flow experiments have been conducted in salt, most of the attempts to simulate them were not combining the knowledge gained from the geomechanical, hydrological and chemical characterization of rock salt behavior. Indeed, these are mostly experiments that took place in the 1990s or earlier, before the advancement of salt coupled processes models and computers necessary for modeling these computationally demanding, highly non-linear coupled processes. The numerical modeling task was further complicated by the poor data quality due to power fluctuations (Krause, 1983), or brine leaks (Coyle et al., 1987), especially in field tests. Hence, uncoupled or loosely coupled models were applied but limited to a qualitative approximation of subsets of the brine inflow data under normal operating conditions. For instance, brine inflow measurements from the isothermal small-scale flow experiment at WIPP were matched using calibrated Darcy's law-based models without integrating geomechanical processes even if they were deemed important (Finley et al., 1992). There were also some attempts to model brine movement under thermal gradients. Coyle et al. (1987) used a liquid and vapor transport model, with a permeability that is several orders of magnitude higher than *in situ* permeability, to simulate the heated brine migration test in Asse mine. As a result, the amount of collected water was overpredicted. Hadley and Faris (1981) also used a water and vapor transport model to match water-release data from the 1-kg salt block test (Hohlfelder and Hadley, 1979). They qualitatively reproduced the brine inflow peaks associated with an increase in heater power level and manually imposed a step increase of permeability/porosity at cooling to reproduce the inflow spike when the heater was shut-down. Besides Hadley and Faris (1981), the cooling phase was generally disregarded in all the other brine migration experiment modeling.

Though a rapid cool down may not occur in a nuclear waste repository environment, a study of cool-down experimental results allows for an enhanced understanding of salt brine flow mechanisms and parameters, especially those describing how permeability changes with mechanical dilation.

The present paper addresses this need for a modeling framework that integrates the knowledge gained in hydrological and geomechanical fields to provide a more rigorous explanation of the experimental data during all the phases, including heating and subsequent cooling. For this purpose, the salt block II laboratory experiment (Hohlfelder, 1980; Hadley, 1981) was chosen given the good quality of the collected temperature and brine inflow data, not only during heating, but also during cooling. Moreover, compared to field tests, it is carried out in a controlled setting that allows to isolate some physical processes and to parametrize the numerical model more effectively. Still, it is challenging to simulate and the two previous attempts to do so : McTigue using a linear thermoporoelastic model (Sherer, 1987), and Ratigan (1984) using a hydraulic model including fluid inclusions movement under thermal gradients, were very limited in terms of results. The model by McTigue (Sherer, 1987) succeeded in reproducing the early stage of the test before heating, whereas Ratigan (1984) presented two scenarios that either highly overestimate or underestimate brine inflow. Again, the cooling phase was not tackled by either of them.

The paper is divided into two main sections. Section 2 presents the THM modeling formalism, implemented in the TOUGH-FLAC simulator (Rutqvist et al., 2002; Rutqvist, 2017; Blanco-Martín et al., 2017), including balance and constitutive equations. In Section 3, the SB II experiment is described as well as the approach used to model it. The effects of heating and cooling on the THM behavior of salt rock are discussed and experimental measurements of temperature in the block and brine inflow at the borehole wall are compared with numerical predictions obtained using the TOUGH-FLAC simulator.

## 2. THM equations of two-phase flow in a deformable porous medium

In this section, mass, energy and momentum balance equations are recalled for a two-phase flow in a deformable porous medium, as well as commonly used constitutive equations and those previously derived to characterize the THM behavior of rock salt barriers in the contexts of storage caverns and radioactive waste disposal in salt rock (Wolters et al., 2012; Blanco-Martín et al., 2015a,b).

We consider that the porous medium (rock salt) is isotropic and composed of an insoluble solid skeleton $\sigma$ encompassing connected intergranular voids through which a liquid phase $\lambda$, and a gaseous phase $\gamma$ circulate. The liquid phase contains two components: water (w) and dissolved air (a) and the gaseous phase is comprised of air (a) and water vapor (w).

In what follows, $T$ is the absolute temperature of all the phases (local thermal equilibrium assumption) and $\phi$ is the eulerian porosity of the porous medium. For each phase $\alpha = \{\lambda, \gamma\}$, $p_\alpha$ denotes its pressure, $\rho_\alpha$ its density, $S_\alpha$ its saturation degree, with $S_\lambda + S_\gamma = 1$, $u_\alpha$ its specific internal energy and $h_\alpha$ its specific enthalpy. The density of the solid skeleton is designated by $\rho_\sigma$ and its heat capacity by $C_{p\sigma}$.

### 2.1. TOUGH-FLAC simulator

The numerical code used in this work is the TOUGH-FLAC simulator. It links TOUGH2 (Pruess et al., 2012), an integral finite difference multiphase flow and heat transport simulator, and FLAC$^{3D}$, a finite-difference geomechanical code (Itasca FLAC3D, 2012). The fixed-stress sequential method (Kim et al., 2011) is used to solve coupled problems. In this method, the energy and mass transfer problem is solved first, under a constant total stress field. Then, the geomechanical problem is solved using the newly calculated fluid phase pressures and saturations and temperature fields (Rutqvist et al., 2002).

**Table 1**
Mass, energy and momentum balance equations.

| Balance equation | $M$ | $F$ | $Q$ |
|---|---|---|---|
| Mass of component w | $\phi\left(S_\lambda\rho_\lambda\chi_\lambda^{\mathrm{w}}+S_\gamma\rho_\gamma\chi_\gamma^{\mathrm{w}}\right)$ | $\rho_\lambda\chi_\lambda^{\mathrm{w}}\overrightarrow{V_\lambda}+\rho_\gamma\left(\chi_\gamma^{\mathrm{w}}\overrightarrow{V_\gamma}+\overrightarrow{J_\gamma^{\mathrm{w}}}\right)$ | – |
| Mass of component a | $\phi\left(S_\lambda\rho_\lambda\chi_\lambda^{\mathrm{a}}+S_\gamma\rho_\gamma\chi_\gamma^{\mathrm{a}}\right)$ | $\rho_\lambda\chi_\lambda^{\mathrm{a}}\overrightarrow{V_\lambda}+\rho_\gamma\left(\chi_\gamma^{\mathrm{a}}\overrightarrow{V_\gamma}-\overrightarrow{J_\gamma^{\mathrm{w}}}\right)$ | – |
| Energy | $\left(1-\phi\right)\rho_\sigma C_{p\sigma}+\phi\left(S_\lambda\rho_\lambda u_\lambda+S_\gamma\rho_\gamma u_\gamma\right)$ | $\overrightarrow{\psi}+\rho_\lambda h_\lambda\overrightarrow{V_\lambda}+\rho_\gamma h_\gamma\overrightarrow{V_\gamma}$ | – |
| Momentum | 0 | $\underline{\underline{\sigma}}$ | $\rho\vec{g}$ |

TOUGH-FLAC has been extended to consider large deformation of the solid (Blanco-Martín et al., 2017), which is of importance in studying the THM behavior of rock salt. Large deformation is taken into account by using the updated Lagrangian approach in which the domain grid is updated at each time step. After every FLAC$^{3D}$ call, the newly calculated strain tensor is used to update the flow properties and the geometrical data in TOUGH2.

The thermodynamic state of liquid and gas phases is calculated using EOS4 module of TOUGH2 (Pruess et al., 2012).

### 2.2. Balance equations

Mass, energy and momentum balance equations can be written under the following general differential form:

$$\frac{\partial M}{\partial t}=-\overrightarrow{\nabla}.F+Q \tag{1}$$

where $M$ is the conserved quantity per unit volume, $F$ its surface flux density and $Q$ a sink or source term per unit volume. Their expressions are gathered in Table 1.

The mass balance equations introduce the mass fractions of components k = {a, w} in phases $\alpha=\{\lambda,\gamma\}$: $\chi_\alpha^{\mathrm{k}}$ with $\sum_{\mathrm{k=a,w}}\chi_\alpha^{\mathrm{k}}=1$. The mass flux of each component is the sum of advective and diffusive terms proportional to $\overrightarrow{V_\lambda}$ and $\overrightarrow{V_\gamma}$, the filtration velocities of phases $\lambda$ and $\gamma$, and $\overrightarrow{J_\gamma^{\mathrm{w}}}$, the diffusive velocity of water vapor in the gas phase $\gamma$, respectively. Diffusion of air in liquid water is neglected. Heat flux is also given by the sum of an advective flux, related to the filtration velocities $\overrightarrow{V_\alpha}$, and a diffusive flux $\overrightarrow{\psi}$. The balance of momentum is derived in terms of the total Cauchy's stress tensor $\underline{\underline{\sigma}}$, under the quasi-static approximation. In the source term $\rho=(1-\phi)\rho_\sigma+\phi S_\lambda\rho_\lambda$ is the bulk density and $\vec{g}$ is the gravity acceleration vector.

The discretization of the mass and energy balance equations using the integral finite difference method in TOUGH2 consists in integrating Eq. (1) over $V_{\mathrm{n}}$, the volume of a grid-block n. By using the divergence theorem, the flux term can be rewritten as an integral over the grid-block surface. And, by replacing the volume integrals with volume averages and the surface integrals with discrete sums over surface averaged segments $A_{\mathrm{nm}}$, common to volume $V_{\mathrm{n}}$ and adjacent volumes $V_{\mathrm{m}}$, the mass/energy balance equations read:

$$\frac{d\left(M_{\mathrm{n}}V_{\mathrm{n}}\right)}{dt}=\sum_{\mathrm{m}}A_{\mathrm{nm}}F_{\mathrm{nm}}+Q_{\mathrm{n}} \tag{2}$$

Grid-block volumes $V_{\mathrm{n}}$ and areas $A_{\mathrm{nm}}$ are updated after each geomechanical calculation in FLAC$^{3D}$ and the term $M_{\mathrm{n}}\frac{dV_{\mathrm{n}}}{dt}$ is computed only at the first iteration of the TOUGH Newton–Raphson run.

### 2.3. Constitutive equations

The balance equations in Section 2.2 need to be supplemented with constitutive equations and state laws.

#### 2.3.1. Complementary equations

We consider that convective fluid flow is induced by pressure gradients only. The phenomenon of intracrystalline fluid inclusions movement under thermal gradients is neglected. Hence, the filtration velocity vectors are given by the following generalized multiphase Darcy's law:

$$\overrightarrow{V_\alpha}=-k\frac{k_{\mathrm{r}\alpha}(S_\alpha)}{\eta_\alpha}\left(\overrightarrow{\nabla}p_\alpha-\rho_\alpha\vec{g}\right),\quad\alpha=\lambda,\gamma \tag{3}$$

where $k$ is the intrinsic permeability tensor, $\eta_\alpha$ is the dynamic viscosity of the $\alpha$-phase and $k_{\mathrm{r}\alpha}$ is the relative permeability of the $\alpha$-phase. The latter is expressed using Corey's curves model (Corey, 1954).

$$\begin{aligned}&k_{\mathrm{r}\lambda}=\hat{S}^4\ \ ;\ \ k_{\mathrm{r}\gamma}=\left(1-\hat{S}\right)^2\left(1-\hat{S}^2\right)\\&\hat{S}=\left(S_\lambda-S_{\lambda\mathrm{r}}\right)/\left(1-S_{\lambda\mathrm{r}}-S_{\gamma\mathrm{r}}\right)\end{aligned} \tag{4}$$

The diffusive velocity vector of water vapor is proportional to the gradient of water mass fraction in gas according to Fick's law :

$$\overrightarrow{J_\gamma^{\mathrm{w}}}=D_\gamma^{\mathrm{w}}\overrightarrow{\nabla}\chi_\gamma^{\mathrm{w}} \tag{5}$$

with $D_\gamma^{\mathrm{w}}$ the molecular diffusion coefficient for component w in phase $\gamma$.

As for the conductive heat flux, Fourier's law is used:

$$\overrightarrow{\psi}=-\Lambda\overrightarrow{\nabla}T \tag{6}$$

where $\Lambda$ is the thermal conductivity of rock salt.

#### 2.3.2. Mechanical constitutive model

To express the stress–strain constitutive relation, the concept of effective stress is used, combined with the partition of the total strain tensor $\underline{\underline{\varepsilon}}$ into an elastic component $\underline{\underline{\varepsilon}}^{\mathrm{e}}$, a non-elastic one $\underline{\underline{\varepsilon}}^{\mathrm{ne}}$ and a thermal component $\underline{\underline{\varepsilon}}^{\mathrm{th}}$. This gives:

$$\underline{\underline{\sigma}}'=\underline{\underline{\sigma}}+B\varpi\underline{\underline{1}}=\mathbf{H}:\left(\underline{\underline{\varepsilon}}-\underline{\underline{\varepsilon}}^{\mathrm{ne}}-A_T T\underline{\underline{1}}\right) \tag{7}$$

where $\underline{\underline{\sigma}}'$ is the effective stress tensor, $A_T$ is the drained linear thermal expansion coefficient, $B$ is the Biot coefficient, $\mathbf{H}$ is the drained elasticity tensor and $\varpi$ is the equivalent pore pressure. The latter is defined as the sum of the product of saturation and pressure of the fluid phases and the interfacial energy (Coussy, 2004), as follows :

$$\varpi=(1-S_\lambda)p_\gamma+S_\lambda p_\lambda+\int_{S_\lambda}^{1}p_{\mathrm{c}}(S)dS \tag{8}$$

with $p_{\mathrm{c}}=p_\gamma-p_\lambda$ the capillary pressure.

The Lux/Wolters constitutive model is used to describe the mechanical behavior of rock salt (Wolters et al., 2012; Blanco-Martín et al., 2016). It defines the drained elasticity tensor as follows:

$$\mathbf{H}=(1-D)\mathbf{H}_0 \tag{9}$$

where $\mathbf{H}_0$ is the Hooke's elasticity tensor of the undamaged rock salt and $0\le D\le 1$ is the damage variable.

The inelastic strain rate tensor in the Lux/Wolters model is the sum of three main components: constant-volume viscous strain rate $\dot{\underline{\underline{\varepsilon}}}_{\mathrm{vp}}$ due to transient and steady-state creep, damage-induced strain rate $\dot{\underline{\underline{\varepsilon}}}_{\mathrm{d}}$ resulting from shear or tensile failure and healing-induced strain rate $\dot{\underline{\underline{\varepsilon}}}_{\mathrm{h}}$.

$$\dot{\underline{\underline{\varepsilon}}}^{\mathrm{ne}}=\dot{\underline{\underline{\varepsilon}}}_{\mathrm{vp}}+\dot{\underline{\underline{\varepsilon}}}_{\mathrm{d}}+\dot{\underline{\underline{\varepsilon}}}_{\mathrm{h}} \tag{10}$$

The viscous component is modeled using a modified version of the constitutive model Lubby2 and includes as well the damage-induced

reduction of the load-bearing cross-sectional area. The parameters characterizing the viscoplastic response vary with the stress state and temperature.

Damage of rock salt occurs when the von Mises equivalent effective stress $\sigma'_v$ exceeds the dilatancy boundary $\beta_{dil}$, which is a function of the minimum principal stress (least compressive) $\sigma'_3$ and the Lode angle $\theta$, or in the presence of tensile stresses:

$$F^{ds} = \sigma'_v - \beta_{dil}\left(\sigma'_3, \theta\right) > 0 \quad \text{or} \quad F^{dt} = 6\langle -\sigma'_3 \rangle > 0 \tag{11}$$

where $\langle . \rangle$ are the Macauley Brackets.

Also, the Lux/Wolters model does not include a tensile cut-off mechanism that prevents tensile stresses from exceeding tensile failure strength (equal to zero in Eq. (11)).

The resulting damage rate is proportional to the sum of the contributions of the shear and tensile yield functions $\left\langle \frac{F^{ds}}{F^*} \right\rangle + \left\langle \frac{F^{dt}}{F^*} \right\rangle$ ($F^* = 1$ MPa).

Shear and tensile damage strain rates are proportional to their respective yield function and to a potential function that dictates the direction of the viscoplastic flow: $Q^{ds} = \sigma'_v - \zeta_{dil}\left(\mathrm{tr}\left(\sigma'\right), \theta\right)$ and $Q^{dt} = F^{dt}$.

This damage can be reduced if the stress state falls below the healing boundary $F^h$ which is expressed as follows:

$$F^h = \Gamma\left(\theta_R, \sigma'_{\perp 1}, \sigma'_{\perp 2}\right) - \sigma'_v \tag{12}$$

The parameters $\theta_R$, $\sigma'_{\perp 1}$ and $\sigma'_{\perp 2}$ are used to characterize the micro-fissures formed as a result of thermo-mechanical damage. They denote, in order, the micro-fissure geometry angle and the stresses within the coordinate system defined by the orientation of the micro-fissures.

The damage rate reduction due to healing is not only a function of $F^h$ but also of the time-dependent variation of micro-fissures angle and direction-oriented stresses. Also, another potential function $Q^h$, solely dependent on $\theta_R$, $\sigma'_{\perp 1}$ and $\sigma'_{\perp 2}$, is used to define the direction of the healing strain rate component.

The full expressions of the yield functions, the potentials, the damage rate and the different strain rate components can be found in Blanco-Martín et al. (2016) and in Wolters et al. (2013). In total, 34 parameters were used to describe all the stages of deformation: elasticity, transient and stationary creep, shear and tensile damage and healing. All these parameters come from Clausthal University of Technology laboratory database based on creep tests and conventional and unconventional triaxial tests conducted on salt samples coming from different salt formations, domal and bedded, from the US and Germany, in wide ranges of stress, strain rate and temperature (Lux et al., 2018).

### 2.3.3. Porosity evolution

In a flow simulation that is not coupled with geomechanics, the mass and energy balance equations in Table 1 are usually supplemented with a simple porosity evolution law featuring the pore volume compressibility $C_p$ and the pore thermal expansivity $\alpha_T$, allowing for a simplified way to account for the deformation of the porous medium due to pore pressure and temperature changes:

$$\delta\phi/\phi = C_p \delta p + \alpha_T \delta T \tag{13}$$

However, this simplified approach may lead to inaccurate results for highly nonlinear coupled problems. When the flow and geomechanics equations are solved sequentially and the domain grid is updated after each geomechanical calculation, the eulerian porosity $\phi$ in the energy and mass balance equations needs to be substituted by its equivalent Lagrangian form $\Phi$, which represents the ratio of the pore volume to the bulk volume in the initial configuration. Moreover, the term proportional to $dV_n/dt$ in mass/energy balance Eq. (2) is computed only in the first iteration of each flow calculation. Hence, to include the volume changes in the other iterations an additional term is added to the variation of the Lagrangian porosity to correct the inconsistency between the flow and the geomechanical problem and to ensure the mass conservation, as follows:

$$\Phi^{i+1} - \Phi^i = \frac{(B^i)^2 + \left(B^i - \phi^i\right)\left(1 - B^i\right)}{K^i_{dr}} \times \sum_{\alpha=\lambda,\gamma} S_\alpha (p^{i+1}_\alpha - p^i_\alpha) + 3\phi^i A_T (T^{i+1} - T^i) - \Delta\Phi_c \tag{14}$$

$$\Delta\Phi_c = \frac{(B^i)^2}{K^i_{dr}} \sum_{\alpha=\lambda,\gamma} S_\alpha (p^i_\alpha - p^{i-1}_\alpha) + 3B^i A_T (T^i - T^{i-1}) - B^i \left( \mathrm{tr}\left(\underline{\underline{\varepsilon}}\right)^i - \mathrm{tr}\left(\underline{\underline{\varepsilon}}\right)^{i-1} \right) \tag{15}$$

where the superscript i indicates time level in time discretization. $K_{dr}$ is the drained bulk modulus and $\mathrm{tr}\left(\underline{\underline{\varepsilon}}\right)$ is the total volumetric strain. They are both updated after each geomechanical calculation in FLAC$^{3D}$.

The details of the establishment of this porosity variation formulation can be found in Kim et al. (2012).

### 2.3.4. Evolution of Biot's coefficient, permeability and capillary pressure

The Biot coefficient is one of the most important parameters to describe the coupling between pore pressure variations and the rock deformation. Due to the low porosity and permeability of undisturbed rock salt, attempts to measure this parameter are scarce. Laboratory experiments conducted by Cosenza et al. (2020) to determine the Skempton's coefficient of undisturbed rock salt of 1% porosity suggested that its Biot's coefficient would be very small, ranging between $2\times10^{-3}$ and $8\times10^{-3}$. However, experimental evidence of the existence of a non negligible hydromechanical coupling characterizing rock salt behavior has been obtained and correlated with micro-fracturing occurrence. Biot's coefficient of rock salt under a stress state in the vicinity of the dilatancy boundary can be as high as 0.25 (Alkan et al., 2007). But, to our knowledge, the evolution of the Biot coefficient of rock salt with the damage level has not been experimentally characterized yet. Hence, in this paper, we assume that the Biot coefficient of undisturbed salt is very low and we consider the following analytical formula to describe its increase with damage (Hou, 2002; Kansy, 2007):

$$B = \max\left(\frac{D}{D_a}, 1 - \exp\left(\frac{\sigma_v m D}{D_a - D}\right)\right) \tag{16}$$

where $m$ is a parameter of the Lux/Wolters constitutive model controlling the influence of the equivalent stress on Maxwell viscosity coefficient (Wolters et al., 2012). The Damage variable $D$ in Eq. (16) is normalized by a value $D_a$, representing the onset of a severely damaged state in a laboratory test, in order to allow $B$ to become equal to 1 when rock salt becomes highly dilated. $D_a$ is taken equal to 0.1 as in Hou (2002).

Thermo-mechanically induced damage leads also to an increase of the intrinsic permeability $k$ that we take into account through the following permeability–dilatancy relationship (Wolters et al., 2012):

$$\begin{cases} \log(k) = \log(k_0) + \left\langle \log\left(\varepsilon_v\right) - \log\left(\varepsilon_{v,0}\right) \right. \\ \qquad \left. + \frac{r}{\ln(10)} \exp\left(s\sigma'_{\perp 2}\right)\left(\mathrm{Ei}\left(t\varepsilon_v\right) - \mathrm{Ei}\left(t\varepsilon_{v,0}\right)\right) \right\rangle \;;\; \varepsilon_v \geqslant \varepsilon_{v,0} \\ k = k_0 \;;\; \varepsilon_v < \varepsilon_{v,0} \end{cases} . \tag{17}$$

where $k_0$ is the initial/minimum salt rock permeability, $\varepsilon_v = \mathrm{tr}\left(\underline{\underline{\varepsilon}}_d + \underline{\underline{\varepsilon}}_h\right)$ is dilatancy, $\varepsilon_{v,0}$ is the dilatancy limit at which damage induced micro-fissures start to coalesce, $\sigma'_{\perp 2}$ is the effective stress perpendicular to the orientation of the micro-fissures, $\mathrm{Ei}(x)$ is the exponential integral function, and $r$, $s$ and $t$ are material constants.

Note that healing of rock salt can lead to a restoration of the undisturbed values of intrinsic permeability and Biot's coefficient.

Furthermore, intrinsic permeability can also increase in the case of a fluid infiltration due to an equivalent pore pressure $\varpi$ that exceeds the minimum principal stress $\sigma_3$ (Wolters et al., 2012). This is likely

to happen when the fluid-saturated rock salt is subjected to high fluid pressure as a result of thermal pressurization in response to high temperatures (e.g. Blanco-Martín et al., 2015a). An empirical formula has been established by Wolters et al. (2012) to describe permeability evolution with pore pressure:

$$\log(k) = i_1 + i_2 \arctan(i_3 \Delta P_{\mathrm{fl}}) + i_4 \exp(i_5 \Delta P_{\mathrm{fl}}) \quad , \quad \Delta P_{\mathrm{fl}} > 0 \tag{18}$$

where $\Delta P_{\mathrm{fl}} = \varpi + \sigma_3$ and $i_1$, $i_2$, $i_3$, $i_4$ and $i_5$ are material parameters.

The changes in permeability and porosity affect the magnitude of capillary pressures. To take account of this, they are scaled using the following formula (Leverett, 1941):

$$p_{\mathrm{c}} = p_{\mathrm{c}_0} \left( \frac{k_0/\phi_0}{k/\phi} \right)^{l} \tag{19}$$

$p_{\mathrm{c}_0}$ is the unscaled capillary pressure, expressed using the van Genuchten model:

$$p_{\mathrm{c}_0} = P_0 \left( [S^*]^{-1/\mu} - 1 \right)^{1-\mu} \quad ; \quad p_{\mathrm{c}0} \geq P_{\max} \tag{20}$$

where $S^* = \left( S_\lambda - S_{\lambda \mathrm{r}} \right) / \left( 1 - S_{\lambda \mathrm{r}} \right)$. Parameters $P_0$, $\mu$, $S_{\lambda \mathrm{r}}$, $P_{\max}$ and $l$ are material constants and $\phi_0$ is the initial porosity of the porous medium.

#### 2.3.5. State laws and saturated/unsaturated state transition

The primary variables used to define the thermodynamic state of the porous medium changes depending on the phase state of the pore fluids. For single phase conditions, the primary variables are pressure $p_\alpha$, air mass fraction $\chi^{\mathrm{a}}_\alpha$ and temperature $T$. In a two-phase condition, the second primary variable is replaced by gas phase saturation $S_\gamma$. The transition from fully saturated to unsaturated porous medium happens when the liquid pressure becomes lower than the sum of the air and vapor partial pressures $p_{\mathrm{a}} + p_{\mathrm{v}}$.

Air partial pressure $p_{\mathrm{a}}$ is related to the mass fraction of air in liquid phase $\chi^{\mathrm{a}}_\lambda$ through Henry's law:

$$p_{\mathrm{a}} = \chi^{\mathrm{a}}_\lambda / \mathrm{H_c} \tag{21}$$

where $\mathrm{H_c} = 10^{-10}$ Pa$^{-1}$ is Henry's constant for air dissolution in water.

Water vapor partial pressure $p_{\mathrm{v}}$ is expressed by Kelvin's equation as a function, not only of temperature, but also of capillary pressure, which is itself a function of saturation (Eq. (20)):

$$p_{\mathrm{v}} = \exp\left( \frac{\mathcal{M}_{\mathrm{w}} p_{\mathrm{c}_0}}{\rho_\lambda \mathrm{R} T} \right) p_{\mathrm{sat}}(T) \tag{22}$$

where $R = 8314.56$ J kmol$^{-1}$ K$^{-1}$ is the universal gas constant, $\mathcal{M}_{\mathrm{w}}$ is the molar mass of water and $p_{\mathrm{sat}}$ is the saturated vapor pressure, which is a function of temperature. The liquid density in Eq. (22) is evaluated at $\left( p_\lambda = p_{\mathrm{sat}}(T), T \right)$.

All the thermodynamic properties of water in its liquid or vapor form (density, specific enthalpy and internal energy, viscosity) are calculated based on the steam table equations as given by International Formulation Committee (1967). The viscosity of the air–vapor mixture is computed from a formulation given by Hirschfelder et al. (1954).

With regard to the density of the gaseous phase, it is calculated as the sum of the densities of dry air and water vapor. Air is assumed to behave as an ideal gas, which allows to derive the following expression of air density $\rho_{\mathrm{a}}$ as a function of temperature $T$ and air partial pressure $p_{\mathrm{a}}$:

$$\rho_{\mathrm{a}} = \frac{\mathcal{M}_{\mathrm{a}}}{\mathrm{R} T} p_{\mathrm{a}} \tag{23}$$

where $\mathcal{M}_{\mathrm{a}} = 28.96$ kg kmol$^{-1}$ is the air molar mass.

The internal energy of the gaseous phase is the sum of the internal energies of air and water vapor weighted by their respective mass fractions, with the change in internal energy of air directly proportional to the change in temperature at constant volume. Their ratio is the specific heat at constant volume $C_{V\mathrm{a}} = 733$ J kg$^{-1}$.

## 3. Application to the SB II experiment

In order to investigate the ability to accurately model multiphase flow induced by heating and cooling in rock salt, the SB II experiment has been chosen. The SB II experiment showed a significant increase of the mass flow rate not only during rock salt temperature increase but also during temperature decrease, and provided temperature and mass inflow measurements of fairly good quality. However, the few numerical studies that attempted to model this experiment provided qualitative interpretations and did not model the cooling phase. To our knowledge, simulations integrating the creep of rock salt and the evolution of the hydromechanical properties have never been undertaken to explain the observed flow surge following both heating and subsequent cooling.

In this section, the experiment is further investigated using a more advanced numerical simulator to provide a better explanation of temperature and inflow measurements. A summary of the experiment is first provided before presenting our numerical simulation approach and the results obtained.

### 3.1. SB II experiment: test description

The Salt Block II experiment was conducted on a cylindrical block, approximately 1 m in diameter and 1 m in height, manufactured out of a large salt block from the Mississippi Chemical Company's potash mine in Southeastern New Mexico. A visual examination of the salt block's outer surface by Lambert (1980) revealed that it was composed primarily of halite (88%), polyhalite (8%), and sylvite (4%). But, the mineralogical analysis of two separate small specimens from the same big block gave different results indicating that this salt deposit has mineralogical variability. Moreover, the block contained between 0.1 and 0.5 weight percent of total volatiles (mainly water) (Hohlfelder, 1980).

A heater emplacement borehole of 0.13 m diameter and 0.8 m depth was drilled from the top center of the cylindrical block and the space between the heater and the borehole walls, was filled with crushed salt. The salt block was then placed in a gas-tight stainless-steel container equipped with cooling coils around its outside circumference, as shown in Fig. 1.

During the test, temperature and heat flux were measured inside the salt block, around the cooling jacket and near the heater using thermocouples (TC) and heat flux gauges. Furthermore, a moisture collection system was used to record brine inflow into the borehole. This system consists of a flow of dry nitrogen gas across the annular space between the heater and the borehole walls, to carry the moisture out in order to collect it. Two methods were used to measure the amount of water carried out by the nitrogen gas. In the first method, temperature, pressure, dew point and flow rate of nitrogen gas were continuously measured at the inlet and exhaust valves in order to calculate the salt block water loss rate. An integration over time of the water loss rate gives the cumulative water loss. The second method consisted of collecting the gas exhaust in downstream desiccant canisters that were regularly weighted before and after each use, and the measured weight difference corresponds to the amount of water carried out by the nitrogen gas. In this case, the water loss rate was obtained through a numerical differentiation of the total water mass over 0.5 day intervals.

The first method was abandoned in the middle of the experiment because of the failure of several dew point measurement gauges. Nevertheless, the comparison of the water loss measurements obtained using the two different methods in the first half of the test showed a fairly good agreement between them and allowed the calibration of the gauges.

The test lasted from November 28, 1978 to April 16, 1979 and comprised five heating stages and a shutdown phase during which heater power was reduced gradually, in three stages, approximately over a month. Over the 4.5 months of the test, two system failures

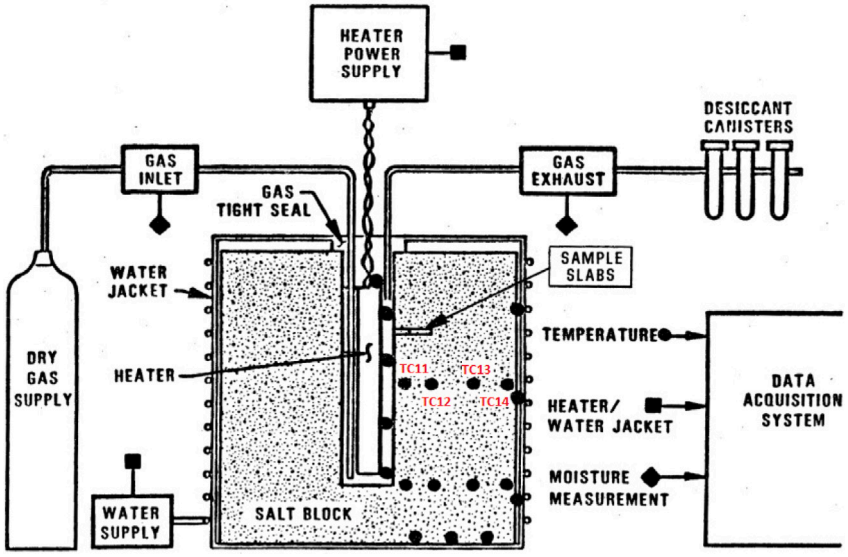


**Fig. 1.** Schematic representation of the laboratory Setup of the Salt Block II experiment (Hohlfelder, 1980). Names of Thermocouples used in this paper have been added.

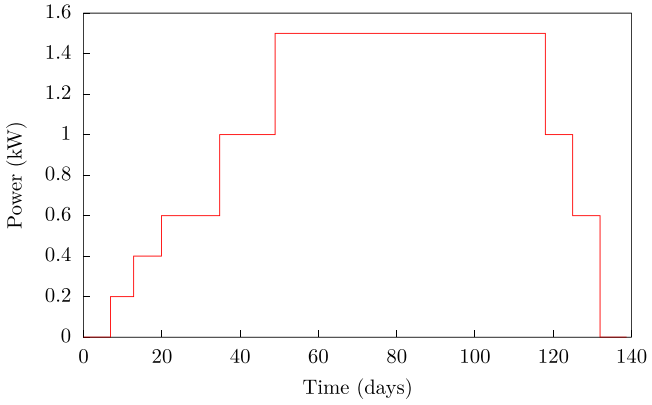


**Fig. 2.** Heater power in SB II experiment (power outage event is not represented).

were reported. The first one was due to a power outage that lasted about 30 min during the 1 kW power stage and entailed an abrupt decrease of the temperature in the salt block. The second one happened 15 days later, during the 1.5 kW stage, due to an interruption of the circumference cooling system that lasted about 16 h and induced a sudden increase of temperature in the salt block. Fig. 2 gives a smoothed history of the heater power, deduced from the chronological order of experimental events given by Hohlfelder (1980). The brief power outage event is not represented in this figure.

### 3.2. Numerical simulations

In this subsection, we present the numerical simulations of the SB II experiment and the comparison between temperature and inflow modeling and experimental results. It is worth mentioning that water inflow in these simulations is solely due to the movement of water through the connected porosity. Fluid flow induced by the movement of fluid inclusions has been neglected in accordance with a mineralogical analysis performed on the salt block at the end of the experiment that indicated a low contribution of intragranular fluid to the total fluid mass loss except within 2 cm of the heater (Lambert, 1980). It also showed that only the larger fluid inclusions located within 7 to 11 cm from the heater are likely to move and change their shape, but they rarely cross grain boundaries and contribute in the collected moisture.

#### 3.2.1. Geometry, initial and boundary conditions and material parameters

Numerical modeling of the SB II experiment has been conducted using an axisymmetric model geometry: a 9° sector model. The displacements in the vertical direction are constrained to plane-strain. Fig. 3 shows a horizontal cross-section of this geometry and the mesh details. In TOUGH-FLAC, the inner boundary is at a radius of 0.065 m (borehole radius), whereas in TOUGH the heater and the annular space are also represented.

We assume that the block is initially brine saturated at 99% and has a uniform initial temperature of 20 °C, a pressure equal to $p_{atm}$ = 0.1 MPa and a total stress of −0.15 MPa. Indeed, because the initial stress state was not measured, its absolute value was set to be somewhat greater than the initial pressure to avoid any infiltration in the first stage of the simulation before the heater is turned-on.

Regarding the boundary conditions, top, bottom and outer boundaries are no-flow. At the borehole wall, relative humidity is equal to 99%, which is equivalent to a capillary pressure of −1.2 MPa. Top and bottom boundaries are thermally insulated whereas temperature at the outer boundary is controlled by the water jacket system which can be best simulated using the following Newton's law of cooling:

$$\vec{\psi}.\vec{n} = h(T - T_c) \tag{24}$$

where $h$ is the convective heat transfer coefficient (W m$^{-2}$ K$^{-1}$), $T_c$ is the coolant temperature, equal to 20 °C, $T$ is temperature of rock salt and $\vec{n}$ is the outward unit vector normal to the outer boundary.

To simulate this thermal boundary condition, an additional grid block is added next to the outer boundary in the TOUGH mesh, with the distance between the centers of the two last grid blocks being $e$ = 2 cm. Temperature is set constant in this new element and thermal conductivity equal to 0.1 W m$^{-1}$ K$^{-1}$. The convective heat transfer coefficient $h$ would be approximately equal to $\lambda/e$ = 5 W m$^{-2}$ K$^{-1}$. Since the heat transfer coefficient between the water cooling system and the salt block was not provided, the value of the thermal conductivity of the outer element was determined based on the maximum temperature that was measured at the surface of the heater hole: 200 °C (Hohlfelder, 1980).

For the mechanical boundary conditions, the inner and outer boundaries are stress and displacement free. The assumption of a free outer boundary is justified by the presence of a 5 mm gap between the salt block and the steel jacket.

Numerical simulations were carried out using parameter values in Table 2. These were identified based on previous research on rock salt (Wolters et al., 2012; Blanco-Martín et al., 2015a, 2016). Remaining parameters of Eqs. (17) and (18) can be found in Wolters (2014).

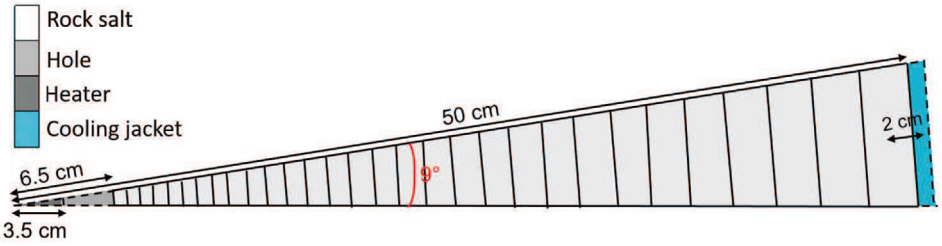


**Fig. 3.** Horizontal cross section of the geometry/mesh. Dashed lines are used to delineate the contour of the geometry in TOUGH.

**Table 2**
Parameters used in numerical simulations.

| Property (unit) | Value |
|---|---|
| Solid density $\rho_\sigma$ (kg/m$^3$) | 2154 |
| Initial porosity $\phi_0$ | 0.001 |
| Initial permeability $k_0$ (m$^2$) | $1\times10^{-21}$ |
| Dilatancy limit $\varepsilon_{v,0}$ | $9\times10^{-4}$ |
| Initial Biot's coefficient | 0.0014 |
| Initial drained bulk modulus $K_{dr}$ (GPa) | 20 |
| Linear thermal expansion coefficient $A_T$ (K$^{-1}$) | $40\times10^{-6}$ |
| Corey's residual liquid saturation $S_{\lambda r}$ | 0.05 |
| Corey's residual gas saturation $S_{\gamma r}$ | 0 |
| Van Genuchten's $\mu$ | 0.6 |
| Van Genuchten's $P_0$ (MPa) | 5.7 |
| Van Genuchten's $S_{\lambda r}$ | 0.01 |
| Parameter $l$ of Eq. (19) | 0.4 |

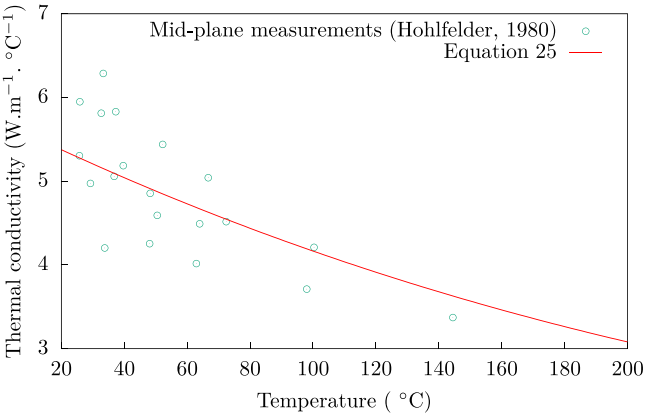


**Fig. 4.** Thermal conductivity of rock salt.

Note that we assigned the salt block a non-zero permeability to account for the damage caused by the mining and drilling processes.

The initial value of the Biot coefficient is assumed to be equal to the lower bound derived by Zimmerman et al. (1986) as a function of porosity: $\frac{3\phi}{2+\phi}$. This gives a Biot's coefficient initial value that is slightly higher than porosity.

To express the evolution with temperature of rock salt heat capacity at constant pressure and thermal conductivity, we use the following empirical formula derived within the BAMBUS project (Bechthold et al., 2004):

$$\begin{cases} C_{p\sigma} = 855 + 0.1777\ T \\ \Lambda = 5.734 - 1.838\times10^{-2}T + 2.86\times10^{-5}T^2 - 1.51\times10^{-8}T^3 \end{cases} . \quad (25)$$

According to these formula, heat capacity at constant pressure increases linearly with temperature and thermal conductivity decreases with an increase of temperature. Moreover, this thermal conductivity expression agrees well with experimental values of the thermal conductivity of the salt block material derived by Hohlfelder (1980) from the measured temperatures and heat fluxes along the mid-plane of the salt block (Fig. 4).

The value of the initial permeability $k_0$ has been fitted to the mass inflow rate in the first stage before the heater was turned on.

The dilatancy limit $\varepsilon_{v,0}$ above which intrinsic permeability of rock salt starts to increase with further thermo-mechanical damage and the maximum value of permeability that can be reached after damage have been fitted to the mass inflow rate measurements.

### 3.2.2. Numerical results and comparison with experimental data

In this section, the computed temperatures and water inflow are discussed and compared with the experimental measurements.

Fig. 5 shows the measured and simulated temperatures for four thermocouples located along the mid-plane of the salt block (see Fig. 1): TC11 (9.2 cm), TC12 (16.8 cm), TC13 (29.5 cm) and TC14 (49.7 cm), for the full duration of the experiment. The agreement between the measurements and the predictions is satisfactory both for heating and cooling, except for the brief variations of temperature due to power outage events during the 4th and 5th heating plateaus which were not simulated. After the interruption of the circumference cooling system at around 60 days, the quality of the temperature predictions in TC14 location deteriorates. Indeed, the impact of any variations in the coolant temperature and in the convective heat transfer coefficient are most noticeable in this thermocouple since it is very close to the outer boundary. It is thus possible that the values of $T_c$ and $h$ prior to this interruption were not exactly restored.

The water inflow rate at the borehole resulting from heating and cooling is shown in Fig. 6. A spike of inflow rate is observed and predicted by the model following any increase or decrease of heater power. The magnitude of the inflow spikes increases with the increase of heater power and is much higher during the cooling phase. After each spike, the inflow rate gradually decreases while temperature has stabilized.

The numerical modeling reveals that the magnitude of the spikes and the subsequent decreasing inflow rate are controlled by a combination of several physical mechanisms. These mechanisms include (1) thermal pressurization generating pressure gradients in the block, (2) fluid viscosity variation with temperature, (3) evolution of relative permeability with temperature-induced desaturation and (4) permeability enhancement due to thermo-mechanical damage.

Figs. 7 and 8 depict the evolution of the change of the equivalent pore pressure (Eq. (8)), the gas pressure and the gas saturation, respectively, in three different points located 6.8 cm, 16.7 cm and 35.7 cm from the center of the borehole. Before heating, the hydraulic boundary condition at the borehole wall is responsible of the changes in the equivalent pore pressure. During heating, the magnitude of the equivalent pore pressure peaks becomes important as we move further away from the borehole. The maximum pore pressure peak amplitude at the 35.7 cm radius is of 0.75 MPa approximately. The simulation results suggest that the desaturation of the salt block is minimal during the heating phase. The most important changes of gas saturation and pressure happen in the point closest to the borehole where the gas saturation reaches 8.2% and the gas pressure 1.6 MPa during the last

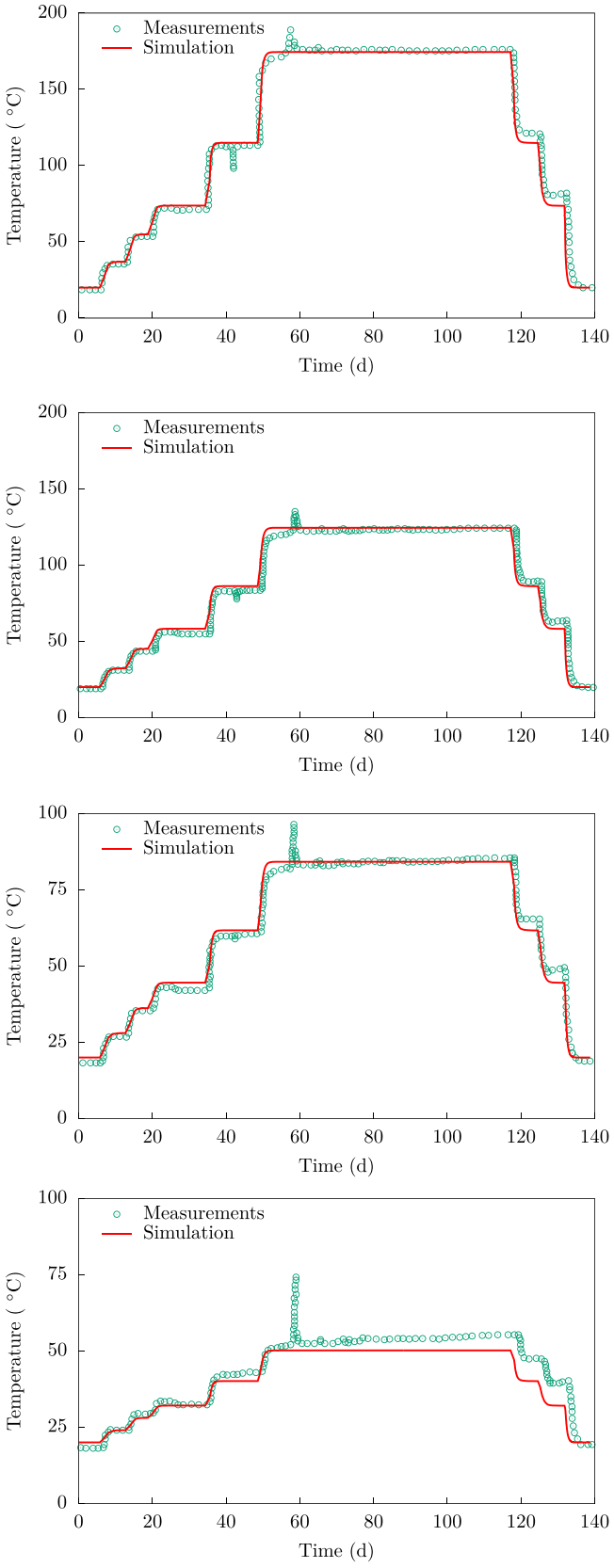


**Fig. 5.** Comparison between measured and predicted temperatures along the mid-plane of the salt block.

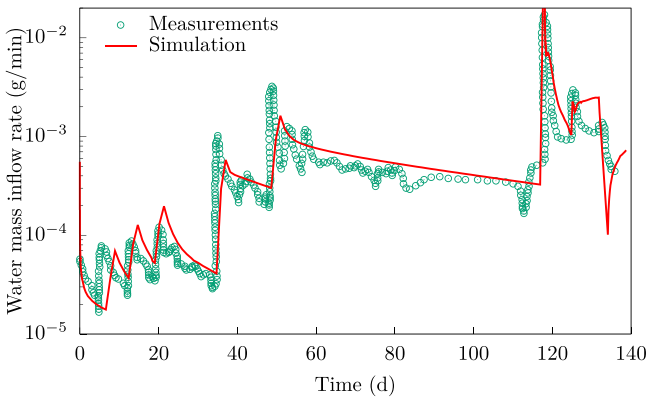


**Fig. 6.** Comparison between measured and predicted evolution of water mass inflow rate at the borehole wall.

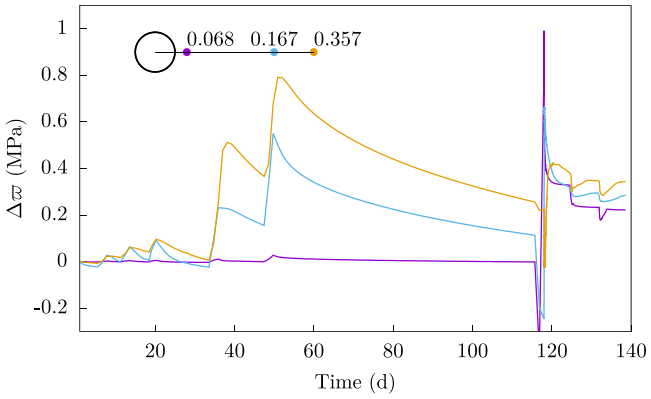


**Fig. 7.** Evolution of the change of the equivalent pore pressure with time at three different locations.

heating step. In the point located 35.7 cm away from the borehole center, the gas saturation starts to visibly increase at around 50 days, but in a way that is not directly correlated with temperature evolution, and gas pressure starts to decrease, contrary to what is predicted in the two other points. The most significant increase of the equivalent pore pressure and the gas saturation in the three points happens when the heater power was decreased for the first time. At the 6.8 cm radius, the gas saturation reaches about 55% and pore pressure increases by 1 MPa, approximately. The equivalent pore pressure immediately starts to decrease which is not the case of the gas saturation. This indicates that the salt block might be irreversibly damaged. Gas pressure decreases, as expected, due to cooling. During the next two cooling steps, small gas saturation peaks are predicted accompanied by small negative peaks of pore pressure.

In order to better understand and complement the information provided by pressure and gas saturation predictions, we need to analyze stress and damage evolution in the salt block. Figs. 9–11 depict the evolution of $\sigma_{xx}$, $\sigma_{yy}$ and the minimum principal stress and Figs. 12 and 13 show the evolution of the damage parameter $D$ and dilatancy. During the heating phase, $\sigma_{xx}$, $\sigma_{yy}$ in the vicinity of the borehole (3 mm) and 10 cm away from the borehole wall are compressive and show a peak each time the heater power is raised, with the peak magnitude increasing with the heater power. Note that any increase of stress is followed by a time-dependent stress relaxation due to salt creep, which is also temperature dependent. Moreover, near the borehole wall, $\sigma_{yy}$ peaks are considerably higher in magnitude than $\sigma_{xx}$ peaks and the opposite is true 10 cm away from the borehole. This big difference between $\sigma_{xx}$ and $\sigma_{yy}$ in both locations is indicative of the presence of important heating-induced shear stresses that would lead to the

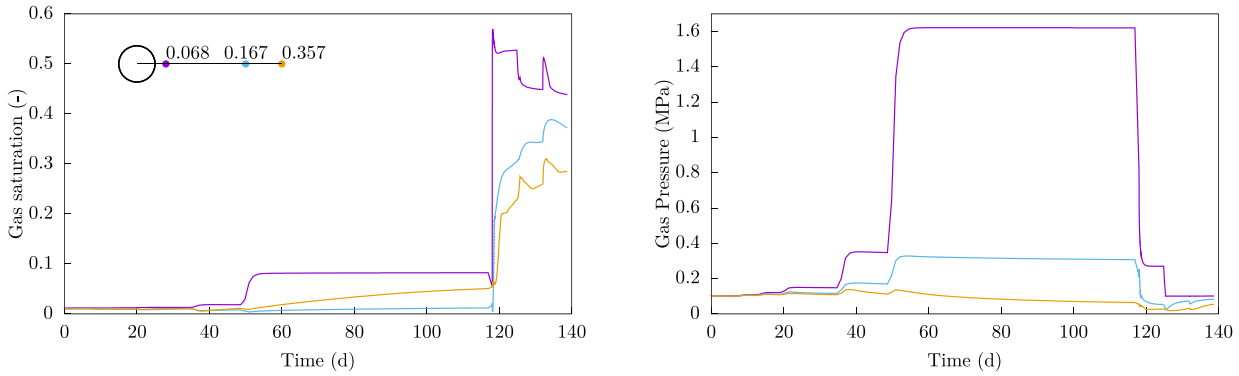


(a) gas saturation (b) gas pressure

**Fig. 8.** Simulated gas saturation and gas pressure evolution with time at three different locations.

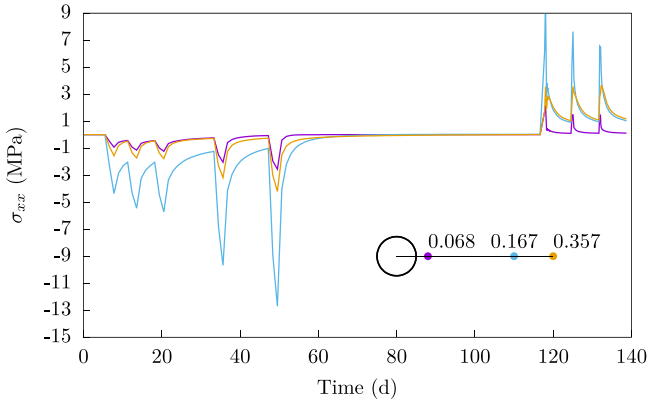


**Fig. 9.** Evolution of $\sigma_{xx}$ with time at three different locations.

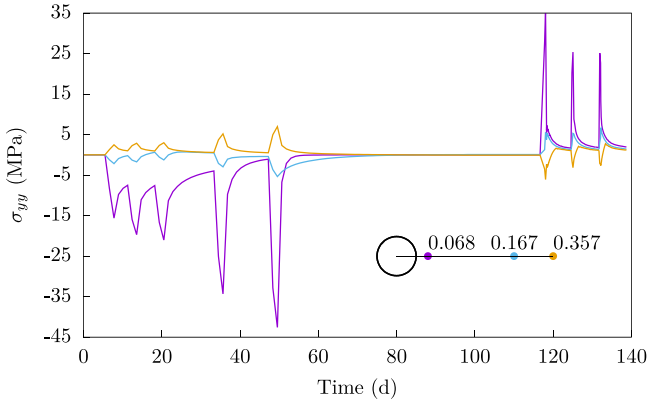


**Fig. 10.** Evolution of $\sigma_{yy}$ with time at three different locations.

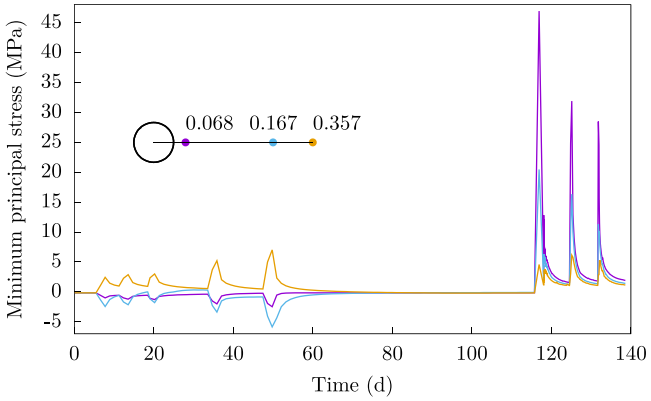


**Fig. 11.** Simulated minimum principal stress evolution with time at three different locations.

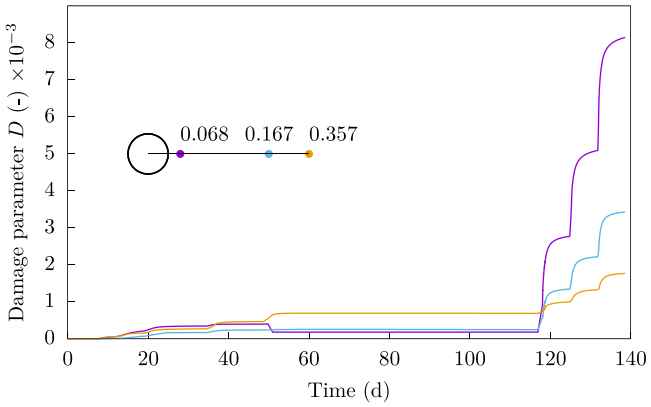


**Fig. 12.** Simulated damage parameter $D$ evolution with time at three different locations.

onset of dilatancy and damage near the borehole wall. Indeed, Fig. 12 shows that damage near the borehole wall starts concomitantly with the second stress peak and a little bit later 10 cm away from the borehole wall. At 50 days, simultaneously with the highest heater power level, Figs. 12 and 13 show a reduction of damage and a decrease of dilatancy below zero near the borehole wall, indicating that the stress state in this location has fallen below the sealing/healing boundary.

Due to the free outer boundary condition, the area located 30 cm away from the borehole wall is subject to tensile stresses, as can be seen in Fig. 11. This results in the onset of tensile-induced dilatancy which is higher than the shear-induced dilatancy predicted in the compressive adjacent area (see Fig. 13).

Turning-off the heater resulted in strong tensile stresses near the borehole (Figs. 9–11) leading to the tensile failure of rock salt and an extensive damage and dilatancy (Figs. 12 and 13) that contributed in a large part to the water loss peaks observed following heater power decreases. A post-mineralogical analysis of the salt block, by Lambert (1980), indicated that the zone most perturbed by temperature variations and from which water was dragged towards the borehole wall occurred within 15 cm of the heater hole. Simulation results show that tensile damage decreases further away from the borehole but extends beyond 30 cm from the borehole wall, as can be seen in

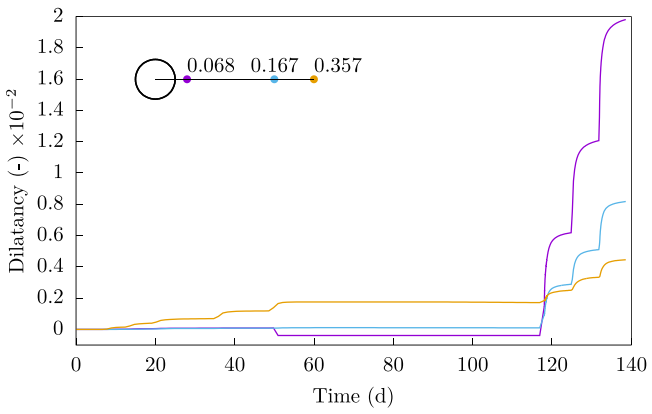


**Fig. 13.** Simulated dilatancy evolution with time at three different locations.

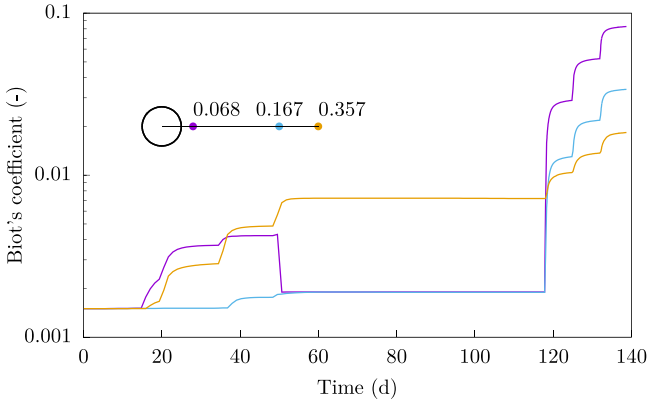


**Fig. 14.** Simulated Biot's coefficient evolution with time at three different locations.

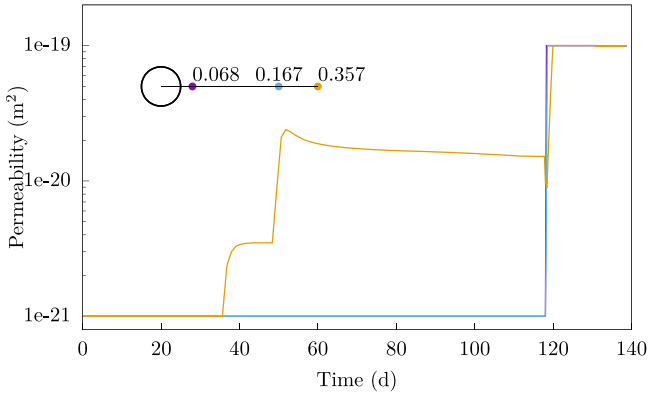


**Fig. 15.** Simulated permeability evolution with time at three different locations.

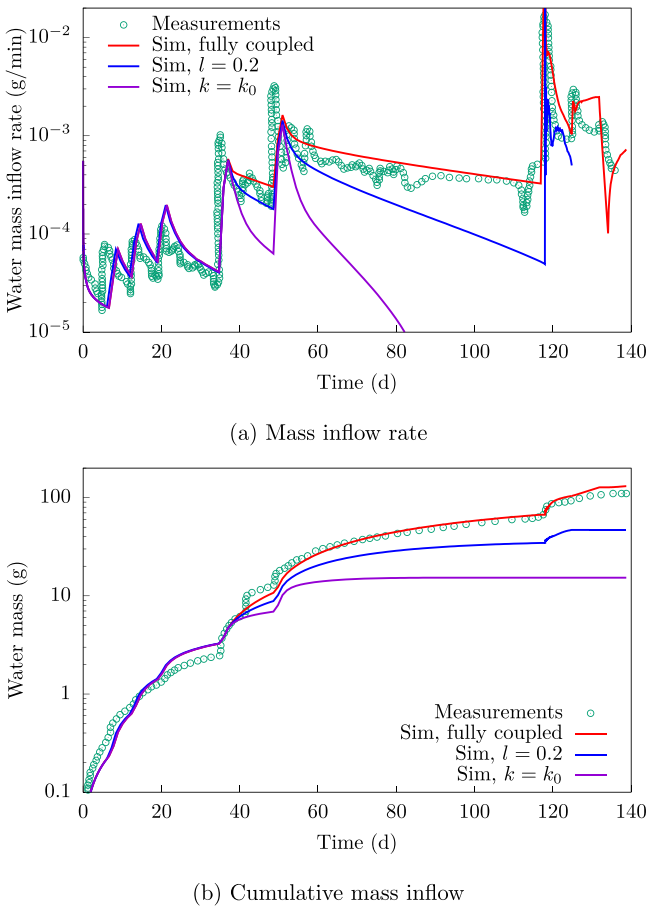


**Fig. 16.** Effect of permeability changes and Leverett scaling of capillary pressure on water inflow.

Fig. 12. Indeed, $\sigma_{yy}$ at 0.357 m radius is compressive during cooling (Fig. 10) but the minimum principal stress remains positive (Fig. 11).

In the model simulations, shear and tensile induced damage resulted in an increase of the Biot coefficient by a factor of 60 (see Eq. (16)) near the borehole by the end of the experiment, as depicted in Fig. 14. Naturally, most of this increase happened during the cool-down phase. Furthermore, when the dilatancy exceeds $\varepsilon_{v,0}$ (see Eq. (17)), permeability increases. Fig. 15 shows that the dilatancy threshold $\varepsilon_{v,0}$ was exceeded first during heating, 35.7 cm away from the borehole center. As a result, permeability increased by a factor of 20, approximately, in this location. This also explains the increasing desaturation and the decreasing gas pressure between 50 and 120 days, shown in Fig. 8 in the same location. Tensile microfracturing of the salt rock during the first cooling step led to a higher dilatancy of the rock (see Fig. 13) and, hence, a substantial increase of permeability in the vicinity of the borehole and an additional increase of permeability in the predamaged areas during heating (35.7 cm radius). A maximum permeability of $1 \times 10^{-19}$ m$^2$ allowed to match the experimental inflow rate which corresponds to an increase of permeability by a factor of 100 at the first cooling step. In the two other cooling steps, permeability remains constant, but rock salt keeps dilating, as can be seen in Fig. 13, which implies changes in porosity and gas saturation, and consequently variations in the capillary pressure (Eq. (19)) and in the equivalent pore pressure.

In order to investigate the contribution of permeability changes and Leverett scaling to the flow rate magnitude, two additional simulations were performed: in the first one, the exponent $l$ in Eq. (19) was reduced from 0.4 to 0.2 which leads to a stronger capillary action, and, in the second one, permeability was kept constant, equal to $k_0$. Fig. 16a and b display the resulting mass inflow rate and cumulative flow together with experimental data and numerical predictions obtained in the fully coupled simulation with variable permeability and $l = 0.4$. The predicted total released water in this reference simulation is in agreement with the experimental observation, which is around 111 g. Also, the cumulative inflow predictions in the heating phase could be enhanced if the power outage event at around 43 days had been properly modeled.

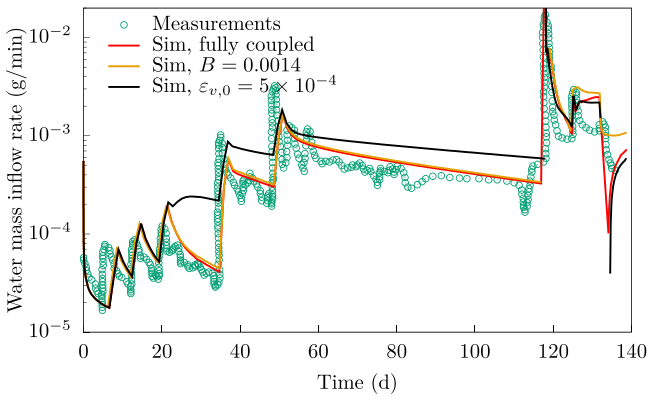


(a) Mass inflow rate

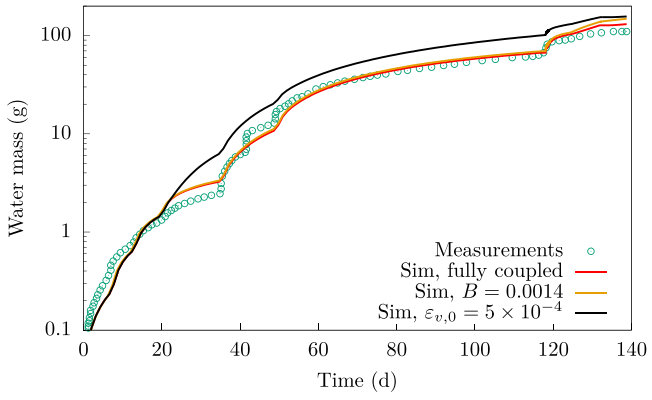


(b) Cumulative mass inflow

**Fig. 17.** Effect of the dilatancy limit $\varepsilon_{v,0}$ and Biot's coefficient $B$ on water inflow.

The two verification simulations show that a constant permeability or a reduction of the Leverett exponent affect the simulated inflow rate starting from about 40 days, time at which permeability increase begins in the reference simulation due to tensile dilatancy. They both lead to a rapid decrease of inflow rate following the 4th and 5th heating inflow spikes. Obviously, no inflow spike happens during cool-down phase if permeability is assumed to remain constant which would result in a significant underestimation of the total released water mass, as shown in Fig. 16b. Leverett scaling also may highly affect water inflow predictions. Indeed, the salt block undergoes a desaturation when porosity and permeability are enhanced due to damage. This is particularly important in the absence of hydrostatic confinement as is the case for the Salt Block experiment.

In addition to that, the impact of the Biot coefficient evolution and the dilatancy limit for the onset of permeability enhancement on the inflow results has also been investigated through two other simulations. Their results are displayed in Fig. 17. In the first simulation the Biot coefficient was kept constant and the inflow results showed that the impact of its evolution with damage is minimal. Indeed, even if the Biot coefficient increased by a factor of 60 in the cooling phase of the reference simulation, its value remained lower than 0.1. In the second simulation, a lower value of the dilatancy limit at which permeability starts to increase was used. This resulted in an early increase of permeability compared to the reference simulation which led to an overestimation of the inflow rates starting from the 3rd peak and an overestimation of the total water mass released in the borehole.

This parametric analysis shows how complex and interrelated the different mechanisms are and the importance of experiments to identify the most predominant mechanisms to consider.

## 4. Conclusion and perspectives

In this paper, we propose a methodology to accurately simulate brine migration in rock salt under heating/cooling induced temperature gradients. For this purpose, the TOUGH-FLAC formulation of non-isothermal multi-component multi-phase flow in deformable porous media was supplemented by appropriate constitutive models that include, in addition to deviatoric creep, viscoplastic volumetric strains and tensile strains, and relationships linking the flow properties to the stresses and the strains. This extended formulation was used to perform thermo-hydro-mechanical simulations of a salt block multistage heating and cooling laboratory test. Simulations allowed to evaluate the predictive capabilities of the TOUGH-FLAC updated formulation and showed the importance of accounting for thermally-activated salt damage and permeability alteration when salt dilates, in both compression and tension, to interpret the brine inflow observations, especially during cooling. Indeed, tensile rock salt failure during cooling entails a significant increase of permeability and a spike of brine inflow with a magnitude exceeding the inflow spikes observed during heating.

However, there are a number of uncertainties in the input material parameters that were either fitted to the inflow rates or determined using salt historical data that is not necessarily representative of the rock salt used in the experiment. More specifically, the increase of the Biot coefficient with damage and its low initial value would benefit from thorough laboratory tests.

Based on our simulations, we highlight the importance of planning and designing a cooling phase instead of a sudden heater turn-off. Indeed, a more gradual reduction of heat power is more representative of the *in situ* conditions in nuclear waste salt repositories. Also, varying cooling rates can help enhance our understanding of cooling-induced damage processes and provide data to constrain the parameters of constitutive models.

Finally, future tests that can represent *in situ* stress and pore pressure conditions will be useful for understanding and controlling repository processes, because tensile failure and damage onset are expected to be less significant under high confining stress.

## CRediT authorship contribution statement

**H. Tounsi:** Methodology, Software, Validation, Visualization, Writing – original draft, Writing – review & editing. **J. Rutqvist:** Conceptualization, Software, Supervision, Writing – review & editing, Funding acquisition. **M. Hu:** Conceptualization, Writing – review & editing. **R. Wolters:** Software, Writing – review & editing.

## Declaration of competing interest

The authors declare that they have no known competing financial interests or personal relationships that could have appeared to influence the work reported in this paper.

## Data availability

Data is already available online

## Acknowledgments

Funding for this work has been provided by the Spent Fuel and Waste Disposition Campaign, Office of Nuclear Energy of the U.S. Department of Energy, under Contract Number DE-AC02-05CH11231 with Lawrence Berkeley National Laboratory.

## References


Alkan, H., Cinar, Y., Pusch, G., 2007. Rock salt dilatancy boundary from combined acoustic emission and triaxial compression tests. Int. J. Rock Mech. Min. Sci. 44 (1), 108–119. http://dx.doi.org/10.1016/j.ijrmms.2006.05.003.

Beauheim, R.L., Roberts, R.M., 2002. Hydrology and hydraulic properties of a bedded evaporite formation. J. Hydrol. 259 (1–4), 66–88, URL: https://doi.org/10.1016/S0022-1694(01)00586-8.

Bechthold, W., Smailos, E., Heusermann, S., Bollingerfehr, W., Bazargan Sabet, B., Rothfuchs, T., Kamlot, P., Grupa, J., Olivella, S., Hansen, F.D., 2004. Backfilling and Sealing of Underground Respositories for Radioactive Waste in Salt: Bambus II Project. Technical Report EUR20621, European Atomic Energy Community.

Blanco-Martín, L., Rutqvist, J., Birkholzer, J.T., 2015a. Long-term modeling of the thermal–hydraulic–mechanical response of a generic salt repository for heat-generating nuclear waste. Eng. Geol. 193, 198–211, URL: https://doi.org/10.1016/j.enggeo.2015.04.014.

Blanco-Martín, L., Rutqvist, J., Birkholzer, J.T., 2017. Extension of TOUGH-FLAC to the finite strain framework. Comput. Geosci. 108, 64–71, URL: https://doi.org/10.1016/j.cageo.2016.10.015.

Blanco-Martín, L., Wolters, R., Rutqvist, J., Lux, K.-H., Birkholzer, J.T., 2015b. Comparison of two simulators to investigate thermal–hydraulic–mechanical processes related to nuclear waste isolation in saliferous formations. Comput. Geotech. 66, 219–229, URL: https://doi.org/10.1016/j.compgeo.2015.01.021.

Blanco-Martín, L., Wolters, R., Rutqvist, J., Lux, K.-H., Birkholzer, J.T., 2016. Thermal–hydraulic–mechanical modeling of a large-scale heater test to investigate rock salt and crushed salt behavior under repository conditions for heat-generating nuclear waste. Comput. Geotech. 77, 120–133, URL: https://doi.org/10.1016/j.compgeo.2016.04.008.

Chen, J., Ren, S., Yang, C., Jiang, D., Li, L., 2013. Self-healing characteristics of damaged rock salt under different healing conditions. Materials 6 (8), 3438–3450, URL: https://doi.org/10.3390/ma6083438.

Corey, A.T., 1954. The interrelation between gas and oil relative permeabilities. Prod. Mon. 38–41.

Cosenza, P., Ghoreychi, M., Bazargan-Sabet, B., De Marsily, G., 1999. In situ rock salt permeability measurement for long term safety assessment of storage. Int. J. Rock Mech. Min. Sci. 36 (4), 509–526, URL: https://doi.org/10.1016/S0148-9062(99)00017-0.

Cosenza, P., Ghoreychi, M., Chanchole, S., 2020. Effects of fluid-rock interaction on mechanical behavior of rock salt. In: Basic and Applied Salt Mechanics. CRC Press, pp. 57–71.

Coussy, O., 2004. Poromechanics. John Wiley & Sons.

Coyle, A., Eckert, J., Kalia, H., 1987. Brine Migration Test Report: Asse Salt Mine, Federal Republic of Germany. Technical Report BMI/ONWI-624, Office of Nuclear Waste Isolation, Columbus, OH (USA).

Ewing, R.I., 1981. Preliminary Moisture Release Experiment in a Potash Mine in Southeastern New Mexico. Technical Report SAND-81-1318, Sandia National Laboratories, Albuquerque, NM (USA).

Finley, S., Hanson, D., Parsons, R., 1992. Small-Scale Brine Inflow Experiments: Data Report Through June 6, 1991. Technical Report SAND-91-1956, Sandia National Laboratories, Albuquerque, NM (USA).

Hadley, G.R., 1981. Salt Block II: Brine Migration Modeling. Technical Report SAND81-0433, Sandia National Laboratories, Albuquerque, NM (USA).

Hadley, G.R., Faris, G., 1981. Revised Theory of Water Transport in Rock Salt. Technical Report SAND80-2398, Sandia National Laboratories, Albuquerque, NM (USA).

Hansen, F.D., 2008. Disturbed rock zone geomechanics at the waste isolation pilot plant. Int. J. Geomech. 8 (1), 30–38, URL: https://doi.org/10.1061/(ASCE)1532-3641(2008)8:1(30).

Hansen, F.D., Leigh, C.D., 2011. Salt Disposal of Heat-Generating Nuclear Waste. Technical Report SAND2011-0161, Sandia National Laboratories, Albuquerque, NM (USA), http://dx.doi.org/10.2172/1005078.

Hirschfelder, J.O., Curtiss, C.F., Bird, R.B., 1954. Molecular Theory of Gases and Liquids. John Wiley & Sons.

Hoffman, E.L., Ehgartner, B.L., 1998. Using Three Dimensional Structural Simulations to Study the Interactions of Multiple Excavations in Salt. Technical Report SAND97-1017C, Sandia National Laboratories, Albuquerque, NM (USA).

Hohlfelder, J.J., 1980. Salt Block II: Description and Results. Technical Report SAND–79-2226, Sandia National Laboratories, Albuquerque, NM (USA).

Hohlfelder, J., Hadley, G., 1979. Laboratory studies of water transport in rock salt. Lett. Heat Mass Transf. 6 (4), 271–279, URL: https://doi.org/10.1016/0094-4548(79)90014-6.

Hou, Z., 2002. Geomechanische Planungskonzepte für Untertägige Tragwerke Mit Besonderer Berücksichtigung Von Gefügeschädigung, Verheilung Und Hydromechanischer Kopplung. Papierflieger, Clausthal-Zellerfeld, Germany.

Hu, M., Rutqvist, J., 2020. Finite volume modeling of coupled thermo-hydro-mechanical processes with application to brine migration in salt. Comput. Geosci. 24 (5), 1751–1765, URL: https://doi.org/10.1007/s10596-020-09943-8.

Hu, M., Steefel, C.I., Rutqvist, J., 2021. Microscale mechanical-chemical modeling of granular salt: Insights for creep. J. Geophys. Res.: Solid Earth 126 (12), e2021JB023112, URL: https://doi.org/10.1029/2021JB023112.

International Formulation Committee, 1967. A Formulation of the Thermodynamic Properties of Ordinary Water Substance. IFC Secretariat, Düsseldorf, Germany.

Itasca FLAC3D, 2012. 5.0 (Fast Lagrangian Analysis of Continua in 3 Dimensions) manual [55401].

Kansy, A., 2007. Einfluss des Biot-Parameters auf das hydraulische Verhalten von Steinsalz unter der Berücksichtigung des Porendruckes (Ph.D. thesis). Technische Universität Clausthal, Clausthal-Zellerfeld, Germany.

Kim, J., Sonnenthal, E.L., Rutqvist, J., 2012. Formulation and sequential numerical algorithms of coupled fluid/heat flow and geomechanics for multiple porosity materials. Internat. J. Numer. Methods Engrg. 92 (5), 425–456, URL: https://doi.org/10.1002/nme.4340.

Kim, J., Tchelepi, H.A., Juanes, R., 2011. Stability and convergence of sequential methods for coupled flow and geomechanics: Fixed-stress and fixed-strain splits. Comput. Methods Appl. Mech. Engrg. 200 (13–16), 1591–1606, URL: https://doi.org/10.1016/j.cma.2010.12.022.

Krause, W.B., 1983. Avery Island Brine Migration Tests: Installation, Operation, Data Collection, and Analysis. Technical Report ONWI-190 (4), Office of Nuclear Waste Isolation, Columbus, OH (USA).

Kuhlman, K.L., Malama, B., 2013. Brine Flow in Heated Geologic Salt. Technical Report SAND2013–1944, Sandia National Laboratories, Albuquerque, NM (USA), URL: https://doi.org/10.2172/1095129.

Lambert, S.J., 1980. Mineralogical Aspects of Fluid Migration in the Salt Block II experiment. Technical Report SAND79-2423, Sandia National Laboratories, Albuquerque, NM (USA), URL: https://doi.org/10.2172/5325528.

Leverett, M., 1941. Capillary behavior in porous solids. Trans. AIME 142 (01), 152–169.

Lux, K., Lerche, S., Dyogtyev, O., 2018. Intense damage processes in salt rock-a new approach for laboratory investigations, physical modelling and numerical simulation. In: Mechanical Behavior of Salt IX. Hannover, Germany, pp. 12–14.

McTigue, D.F., Nowak, E.J., 1987. Brine Transport Studies in the Bedded Salt of the Waste Isolation Pilot Plant (WIPP). Technical Report SAND-87-1274C, Sandia National Laboratories, Albuquerque, NM (USA).

Pruess, K., Oldenburg, C., Moridis, G., 2012. TOUGH2 User's Guide, Version 2.0. Report LBNL-43134.

Ratigan, J., 1984. A finite element formulation for brine transport in rock salt. Int. J. Numer. Anal. Methods Geomech. 8 (3), 225–241, URL: https://doi.org/10.1002/nag.1610080303.

Rouabhi, A., Hévin, G., Soubeyran, A., Labaune, P., Louvet, F., 2017. A multiphase multicomponent modeling approach of underground salt cavern storage. Geomech. Energy Environ. 12, 21–35, URL: https://doi.org/10.1016/j.gete.2017.08.002.

Rutqvist, J., 2017. An overview of TOUGH-based geomechanics models. Comput. Geosci. 108, 56–63, URL: https://doi.org/10.1016/j.cageo.2016.09.007.

Rutqvist, J., Wu, Y.-S., Tsang, C.-F., Bodvarsson, G., 2002. A modeling approach for analysis of coupled multiphase fluid flow, heat transfer, and deformation in fractured porous rock. Int. J. Rock Mech. Min. Sci. 39 (4), 429–442, URL: https://doi.org/10.1016/S1365-1609(02)00022-9.

Schulze, O., Popp, T., Kern, H., 2001. Development of damage and permeability in deforming rock salt. Eng. Geol. 61 (2–3), 163–180, URL: https://doi.org/10.1016/S0013-7952(01)00051-5.

Shefelbine, H.C., 1982. Brine migration: A summary report. Technical Report SAND82-0152, Sandia National Laboratories, Albuquerque, NM (USA).

Sherer, N.M. (Ed.), 1987. Proceedings of Salt Repository Project's Workshop on Brine Migration. Technical Report PNL/SRP-SA-14341, Pacific Northwest National Laboratory.

Stormont, J., 1997. In situ gas permeability measurements to delineate damage in rock salt. Int. J. Rock Mech. Min. Sci. 34 (7), 1055–1064, URL: https://doi.org/10.1016/S1365-1609(97)90199-4.

Stormont, J., Daemen, J., Desai, C., 1992. Prediction of dilation and permeability changes in rock salt. Int. J. Numer. Anal. Methods Geomech. 16 (8), 545–569, URL: https://doi.org/10.1002/nag.1610160802.

Sweet, J., McCreight, J., 1983. Thermal conductivity of rocksalt and other geologic materials from the site of the proposed waste isolation pilot plant. In: Thermal Conductivity, Vol. 16. Springer, pp. 61–78.

Winterle, J., Ofoegbu, G., Pabalan, R., Manepally, C., Mintz, T., Pearcy, E., Fedors, R., 2012. Geologic Disposal of High-Level Radioactive Waste in Salt Formations. Technical Report NRC-02-07-006, US Nuclear Regulatory Commission.

Wisetsaen, S., Walsri, C., Fuenkajorn, K., 2015. Effects of loading rate and temperature on tensile strength and deformation of rock salt. Int. J. Rock Mech. Min. Sci. (73), 10–14, URL: https://doi.org/10.1016/j.ijrmms.2014.10.005.

Wolters, R., 2014. Thermisch-Hydraulisch-Mechanisch Gekoppelte Analysen zum Tragverhalten von Kavernen im Salinargebirge vor dem Hintergrund der Energieträgerspeicherung Und Der Abfallentsorgung: Ein Beitrag zur Analyse von Gefügeschädigungsprozessen und Abdichtungsfunktion des Salinargebirges im Umfeld Untertätiger Hohlräume (Ph.D. thesis). Technische Universität Clausthal, Clausthal-Zellerfeld, Germany.

Wolters, R., Lux, K.-H., Düsterloh, U., 2012. Evaluation of rock salt barriers with respect to tightness: influence of thermomechanical damage, fluid infiltration and sealing/healing. In: Mechanical Behaviour of Salt VII. CRC Press, pp. 439–448.

Wolters, R., Lux, K.-H., Rutenberg, M., et al., 2013. Load-bearing behaviour of sealed caverns in rock salt used for disposal of hazardous waste. In: 47th US Rock Mechanics/Geomechanics Symposium.

Zhang, H., Huang, Z., Zhang, S., Yang, Z., Mclennan, J.D., 2020. Improving heat extraction performance of an enhanced geothermal system utilizing cryogenic fracturing. Geothermics 85, 101816, URL: https://doi.org/10.1016/j.geothermics.2020.101816.

Zimmerman, R.W., Somerton, W.H., King, M.S., 1986. Compressibility of porous rocks. J. Geophys. Res.: Solid Earth 91 (B12), 12765–12777, URL: https://doi.org/10.1029/JB091iB12p12765.